Journal of
Marine Science and Engineering

MDPI

Article

Distribution Analysis of Local Ice Pressures in the Indentation Test at Various Velocities

Guojun Wang [1], Qianjin Yue [2], Dayong Zhang [2,*], Yanghua Fu [2], Xin Peng [2] and Rui Dong [2]

1 Department of Mechanical Engineering, Dalian University of Technology, Dalian 116000, China; wgjung@mail.dlut.edu.cn
2 School of Ocean Science and Technology, Dalian University of Technology, Panjin 124000, China; yueqj@dlut.edu.cn (Q.Y.); fyhneo2221@mail.dlut.edu.cn (Y.F.); pengxin0610@mail.dlut.edu.cn (X.P.); dongrui007@mail.dlut.edu.cn (R.D.)
* Correspondence: zhangdy@dlut.edu.cn

Abstract: When sea ice acts on vertical structures, there are much higher pressures in localized areas known as high-pressure zones (HPZs) than in other areas. The damage failure mode of sea ice varies with the sea ice velocity and affects the distribution of HPZs. In this study, an indentation test that drives ice sheet interaction with a vertical rigid plate (indentor) was designed, and a pressure sensor (consisting of 32 × 32 small pressure units of 100 mm^2) was installed on the indentor face to measure the local ice pressure (LIP) at various velocities. The distribution of the LIPs along the ice thickness, the probability distribution of the LIPs and the distribution relationship of the LIPS in space and time were obtained from the measurement. The results show that the LIPs were mainly distributed in the middle of the sea ice, which is consistent with full-scale observations and previous research. Ductile failure of the sea ice results in a larger LIP distribution area than brittle failure at the same threshold k_t ($k_t = \sigma_L/\sigma_{cr}$). The probability distribution of the LIPs decreases exponentially with increasing pressure and follows a lognormal distribution. The maximum LIP appears at the peak moment of the global force when the sea ice failure mode is mainly ductile failure. However, the maximum LIP may not occur at the peak moment when the sea ice failure is mainly brittle failure and, instead can appear at any moment in the global force time history curve. The HPZ (which is larger than 7/8 times the maximum LIP) area is less than 2% of the nominal contact area at various velocities. The influence of the sea ice velocity on the spatial and temporal distribution of LIP is analyzed, and the results provide a reference for designing structures with local strength in ice regions.

Keywords: local ice pressure; sea ice failure mode; distribution of local ice pressures; probability distribution

Citation: Wang, G.; Yue, Q.; Zhang, D.; Fu, Y.; Peng, X.; Dong, R. Distribution Analysis of Local Ice Pressures in the Indentation Test at Various Velocities. *J. Mar. Sci. Eng.* **2022**, *10*, 433. https://doi.org/10.3390/jmse10030433

Received: 21 January 2022
Accepted: 15 March 2022
Published: 16 March 2022

1. Introduction

The sea ice failure mechanism is a complex process when it interacts with vertical structures. The failure mode is affected by the interaction velocity, sea ice properties and structural characteristics. Uniaxial compression tests on sea ice reveal brittle failure behavior at low strain rates (less than 10^{-4} s^{-1}) and ductile failure behavior at high strain rates (greater than 10^{-2} s^{-1}) [1,2]. Different failure modes directly affect the local ice pressures (LIPs). Observations show that the pressure is much higher in localized areas than elsewhere when sea ice acts on vertical structures [3–6], and it is necessary to clarify the local ice force when designing structures. Because effective models for the distribution characteristics of high-pressure zones (HPZs) (value, area size, number, location, etc.) are generally lacking, in structure design, the spatial average of the global force is typically used as the ice pressure that acts on the nominal contact surface [7,8].

The effect of HPZs on the structural local response is an important factor to consider. HPZs are highly random in both time and space and result in a significant maximum LIP [7]. The following factors may account for this situation: (1) the contact between the sea ice and the structure surface is non-simultaneous, and the sea ice failure is also non-simultaneous; and (2) the breaking strengths of the sea ice at local contact points are not necessarily the same. Based on experimental and field-measured ice force data, Sanderson [9] analyzed the trend of decreasing effective pressure with increasing contact area. Within addition to the data summarized by Sanderson, many scholars have studied the relationship between local ice pressure and local area and obtained their own results. Most of the results show that LIPs decrease with increasing contact area [10–14]. The relationship between LIP and contact area can be described by a power law. The maximum LIP occurs at a small point in the nominal contact area. When the width of the structure is much greater than the thickness of the sea ice, the failure of the sea ice in these two directions will differ due to different lateral ice restrictions. Under the action of the lateral limiting force, the extrusion and crushing characteristics are changed such that the HPZs are distributed in the center of the ice thickness, and the LIP near the free surface is lower. Some scholars have described this distribution of HPZs, which is mainly in the middle of the ice thickness, as line-like contact, and some methods to explain this characteristic have been proposed [3,5,15,16]. Jordaan [16] conducted a detailed analysis of the influence of the ice breaking process on LIPs and found that the ice has a triaxial stress state that varies from low confinement near the edges to high contact pressures near the center. Dempsey et al. found that the HPZs seem to be confined to the middle third of the ice thickness (ice thickness is less than 0.6 m) [3].

Considering that the failure mode of sea ice is necessary for studying the scale effect of sea ice, at different ice velocities, sea ice exhibits ductile failure or brittle failure. Sodhi proposed that the change in effective ice pressure is mainly affected by the failure mode of the sea ice; that is, whether the sea ice experiences ductile failure or brittle failure [5]. Full-scale tests and small-scale tests have shown that the failure mode of the sea ice, rather than the size of the contact surface, effectively reflects the interaction between the ice and the structure. At low loading speeds, the sea ice is mainly in ductile failure mode, with one or more cleavage cracks forming at different depths of the ice sheet, and the sea ice breaks into fragments and powder and is extruded from the upper and lower surfaces [17–21]. At high loading speeds, the sea ice is mainly in brittle failure mode, with the sea ice forming wedge-shaped crushing cracks. Then, the sea ice splits and spalls on the upper and lower surfaces due to the cracks [20,22,23]. This results in different pressure distributions. Taylor et al. proposed a probabilistic HPZ modes and a probabilistic fracture mechanics model for local pressures based on Japan Ocean Industries Association (JOIA) medium-scale test data [8,24]. The loading speed considered in their studies are 3 mm/s and 30 mm/s. More works about LIP spatial and time distributions relationship and area sizes at various velocities should be considered.

The above discussion indicated that the load speed is one of the main factors affecting the distribution of LIPs. The study discussed provides a reference for further research on HPZs. Based on the different failure modes of sea ice at various loading speeds, this paper studies the local ice pressure distribution of sea ice ductile failure at low ice velocities and brittle failure at high ice velocities. The effects of different failure modes on the distribution of local ice pressure on ice thickness and structure width are analyzed. Combined with the probability model, the distribution characteristics of the LIP are discussed. The spatial distribution characteristics of the HPZ are discussed at different ice failure models.

2. Crush Failure Characteristics of Sea Ice

There are bubbles, brine and impurities in sea ice, which cause defects in the sea ice microstructure. In the uniaxial compression test, the sea ice shows ductile failure characteristics when the strain rate is less than 10^{-4} s^{-1}. The sea ice shows brittle failure characteristics when the strain rate is greater than 10^{-2} s^{-1}. The sea ice also shows characteristics of the ductile-brittle transition at the transition rate. The compressive strength of the sea ice generally reaches its maximum value in this range [1,2,25]. At a low loading rate, the sea ice releases strain energy through creep expansion deformation. With increasing loading rate, the internal microcracks expand rapidly and fracture, showing a transition from ductile failure to brittle failure.

2.1. Ductile Failure

At a low strain rate (less than 10^{-4} s^{-1}), the initial cracks are generated in the sea ice (as shown in Figure 1a,b). With continuous loading, the sea ice deforms, and the microcracks develop into wing cracks that are not always parallel to the loading direction. The horizontal tensile stress promotes the vertical growth of cracks. Due to the slow increase in stress, the stress concentration at the crack tip can be released by creep relaxation, preventing it from growing, and thus brittle failure does not occur (as shown in Figure 1a,b). The experimental results are similar to those of Chen et al. [26].

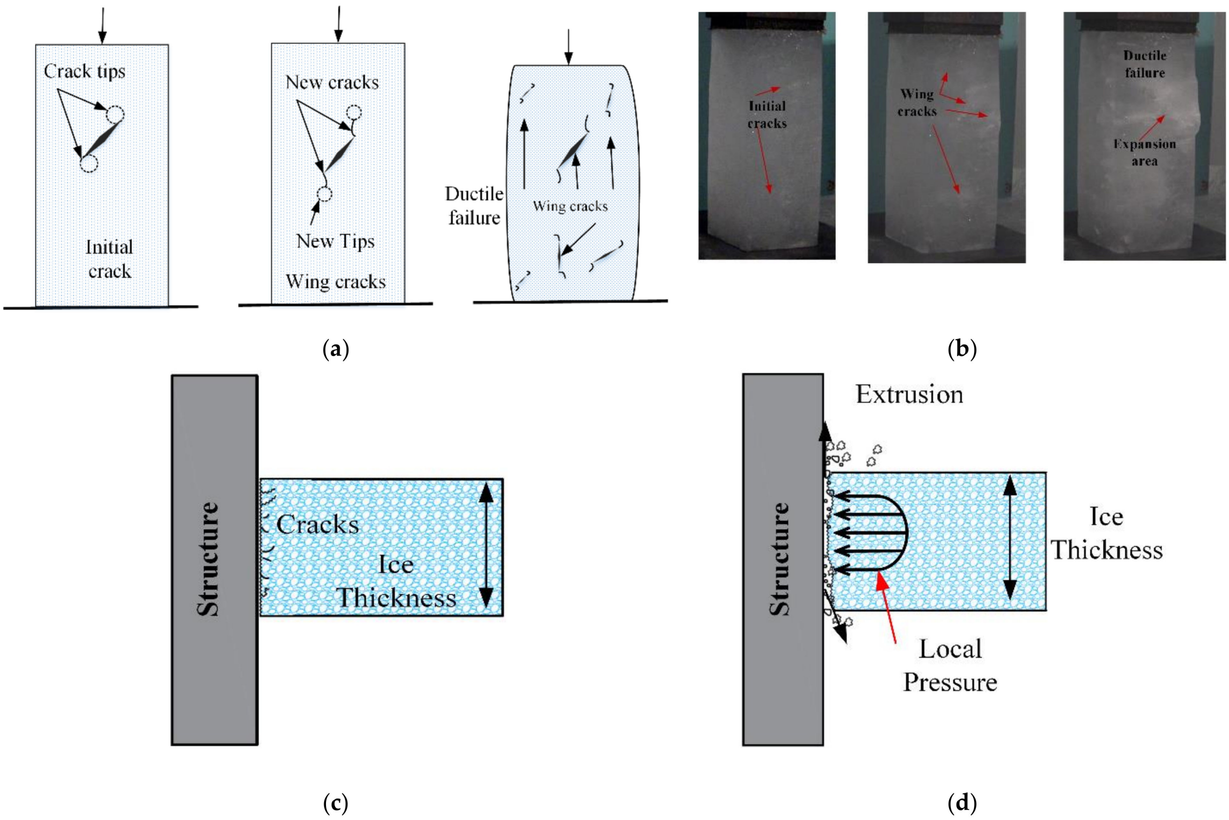

Figure 1. Crack growth at a low loading speed and the theoretical crushing process in front of the vertical structure. (**a**) Schematic of internal crack propagation, (**b**) Uniaxial compressive test at a strain rate of 10^{-4} s^{-1}, (**c**) Initial crack formation in the sea ice in front of the structure, (**d**) Local ice pressure and ice fragmentation extrusion.

Figure 1c,d show that multiple wing cracks form in the sea ice during the later stages of loading. Creep behavior dominates, exhibiting ductile failure characteristics. The ice specimen expands and deforms macroscopically. Based on the ductile failure characteristics of the sea ice, when the interaction velocity between sea ice and the vertical structure is low, many microcracks are produced in the near-field ice in front of the structure. The internal cracks are evenly distributed, and the sea ice breaks into small fragments or powder. In the direction of the ice thickness, the broken ice may extrude from the upper and lower free surfaces in fluid form. Under the influence of the lateral limiting force, the HPZs are distributed close to the center of the ice thickness (Figure 1c,d).

2.2. Brittle Failure

At a high strain rate (greater than 10^{-4} s^{-1}), the initial microcrack development is similar to that at a low strain rate. Microcracks appear during the initial stage and develop into wing cracks. Due to the high strain rate, the stress concentration at the tip of the wing cracks cannot be completely released by creep. Due to stress concentration, the stress path of the specimen develops mainly around the crack, forming a yield surface (as shown in Figure 2a,b). Wing cracks will develop into primary cracks macroscopically along the crack to the free surface, splitting the ice (Figure 2b). The experimental results are similar to those of Chen et al. [26].

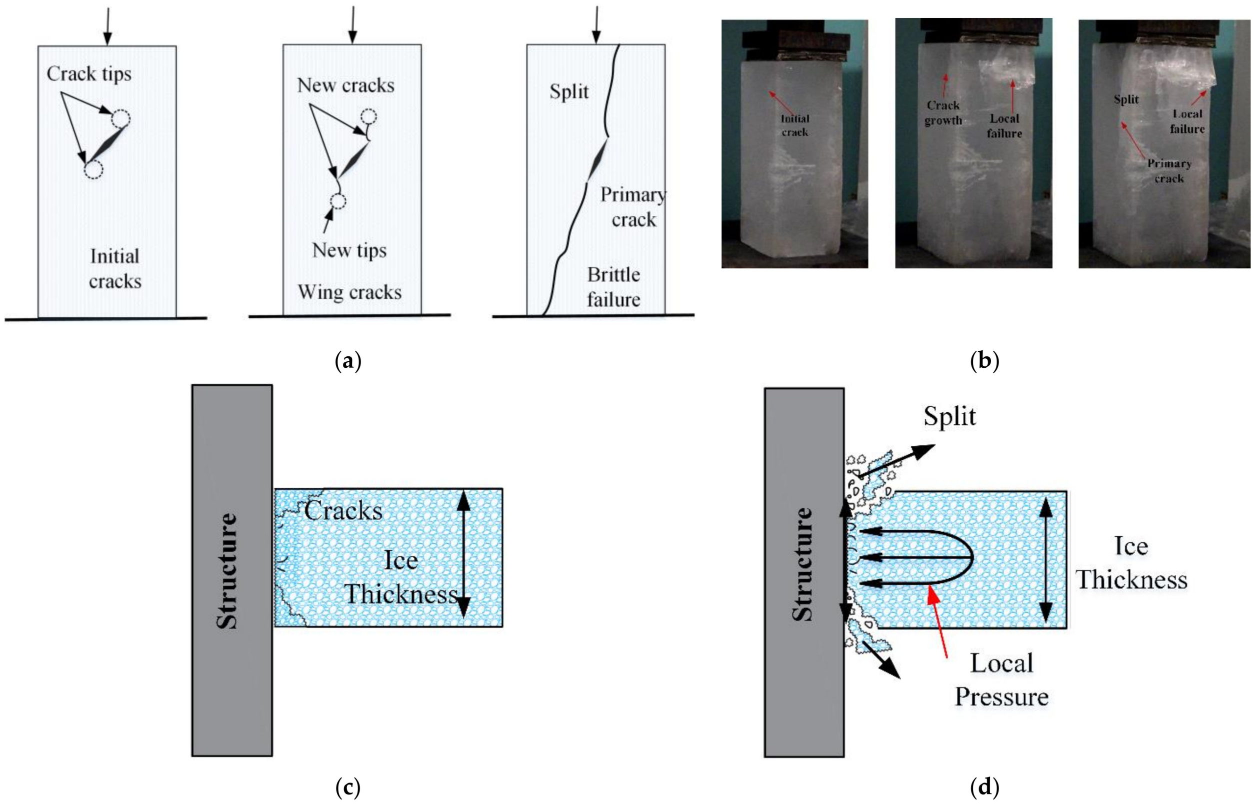

Figure 2. Crack growth at low loading speeds and the theoretical crushing process in front of the vertical structure. (**a**) Schematic of internal crack propagation, (**b**) Uniaxial compressive test at a strain rate of 10^{-4} s^{-1}, (**c**) Initial crack formation in the sea ice in front of the structure, (**d**) Local ice pressure and ice fragmentation extrusion.

Figure 2c,d shows that as the interaction velocity between the sea ice and the structure increases, the near-field ice in front of the structure mainly experiences brittle failure, with some sea ice breaking into blocks (near the free surface), and some breaking into fragments or powder (near the center). The broken ice at the center extrudes from the upper and lower free surfaces. The HPZs are mainly distributed in the central area, with the probability of HPZs decreasing farther from the center. The effective contact area in brittle failure is smaller than that in ductile failure.

The analysis revealed that along the direction of the sea ice thickness, the ice pressure is concentrated in the center of the ice thickness. The above discussion indicated that the ice velocity affects the sea ice failure mode during the sea ice/structure interaction, and the distribution of LIPs in the direction of the ice thickness differs when the sea ice failure mode changes. To further clarify the distribution of LIPs when the sea ice acts on structures at various velocities, an indentation test that drives ice sheet interactions with a vertical rigid plate (indentor) was designed. This test can be used to measure the LIP values and distributions.

3. Indentation Test of Sea Ice Acting on a Structure

The indentation test is a small-scale experiment. The test system includes a pressure sensor (model number: MF-3232, produced by Suzhou LEANSTAR company, Suzhou, China, consisting of 32 × 32 small pressure units of 1 cm^2) on the face of the indentor, and the local ice pressure (LIP) was measured at various velocities. The distribution of the LIPs along the ice thickness, the probability distribution of the LIPs and the distribution of the LIPs in space and time were obtained from these measurements.

3.1. Indentation Test Device

Figure 3a shows a schematic diagram of the indentation test device, and consist of the followings: 1. rigid plate (indentor), which is fixed to the ground and has a contact width of 500 mm with the ice sheet; 2. thin-film pressure transducer, which is attached to the indentor surface (the acquisition area is 320 mm × 320 mm (the nominal contact width (NCW)), the acquisition frequency is 25 Hz, the acquisition accuracy is 0.001 MPa) (Figure 3c); 3. ice sheet, with a size of 1750 mm × 1000 mm, freezes the ice in the ice box; 4. support platform, which holds the ice box; 5. ice box, which is used to freeze the ice and has a size of 1750 mm × 1000 mm × 200 mm, with a notch (520 mm × 550 mm) in the middle of the ice box so that the ice can act on the indentor and a slide rail installed at the bottom and installed on the support platform; 6. thermocouple sensor, which is used to measure the temperature of the ice sheet during ice freezing; and 7. hydraulic actuator, which has a maximum thrust of 50 kN and drives the ice sheet interaction with the indentor. Sea salt was used to prepare high-salinity seawater in the ice box to reduce the ice strength. The brine water was frozen by rapidly cooling to −20 °C, and then rewarmed to bring the internal temperature of the ice sheet to −7 °C or −8 °C (Figure 3b,d).

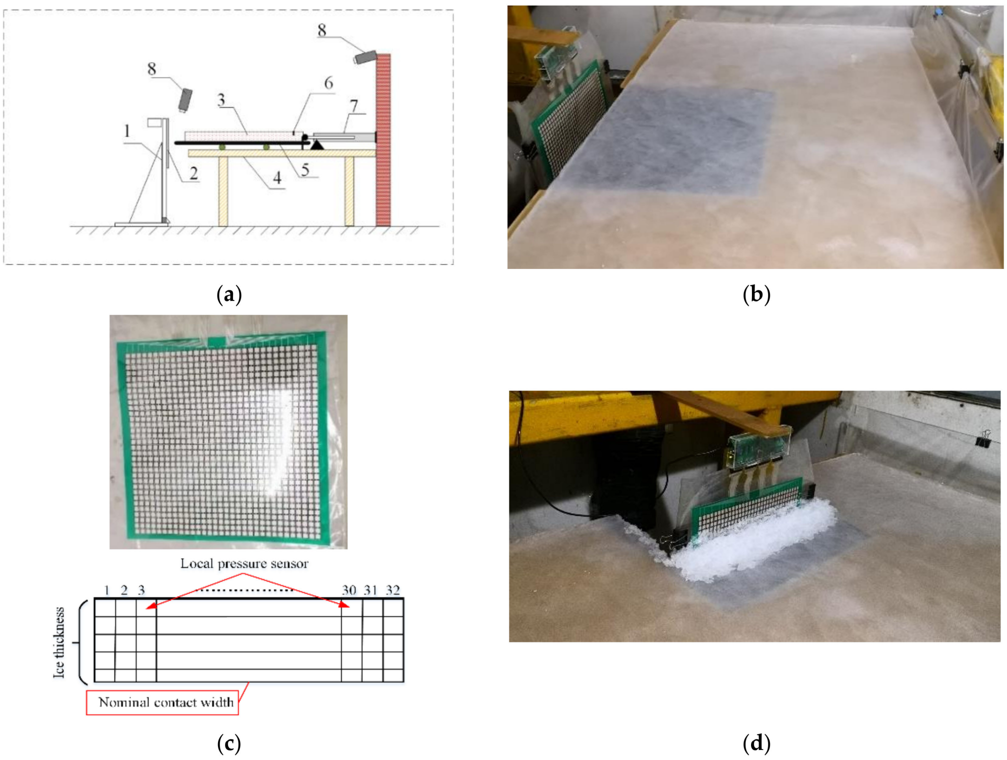

Figure 3. Indentation test device and schematic. (**a**) device schematic; (**b**) device and frozen ice sheet; (**c**) thin-film pressure transducer; (**d**) test load.

To simulate the different failure characteristics of the sea ice, the actuator was set to five different loading velocities (V_{load}: 1 mm/s, 4 mm/s, 7 mm/s, 15 mm/s, and 30 mm/s), causing the ice sheet to act on the indentor at a corresponding velocity. The thin-film pressure transducer was attached to the indentor surface so that it was in direct contact with the ice sheet. The ice pressure values at different positions of the indentor were obtained by direct measurements. After the loading test, the specimens for the uniaxial compression test were cut from the ice sheet to determine the compression strength. The main test parameters are listed in Table 1.

Table 1. Parameters of the indentation test.

Specimen	S (‰)	h_{ice} (mm)	T_{ice} (°C)	V_{load} (mm/s)	σ_{cr} (MPa)	Failure
0516-v1	26	55	−9.3	1	0.553	ductile
0531-v1	31	42	−8.8	1	0.351	ductile
0602-v7	28	60	−8	7	0.287	mixed
0606-v4	30	65	−9.3	4	0.362	ductile
0606-v15	33	65	−7.2	15	0.221	brittle
0609-v15	33	63	−8.2	15	0.336	brittle
0611-v30	29	65	−8	30	0.358	brittle
0724-v30	23	44	−7.0	30	0.232	brittle

S—Salinity of ice; h_{ice}—Average thickness of the ice sheet; T_{ice}—Average ice temperature; V_{load}—Loading velocity; σ_{cr}—Average uniaxial compression strength of the ice sheet.

3.2. Local Ice Pressures and Global Ice Force

Because the ice sheet is frozen in the ice box, the front of the ice sheet is smooth and flat. Simultaneous crushing occurs when the ice plate interacts with the structure during the initial stage. The global ice force data shows that the first peak force is much larger than the subsequent peak (as shown in Figure 4). As loading progresses, the subsequent crushing section is no longer flat, the crushing after the first peak exhibits non-simultaneous crushing characteristics, and the value of the peak force decreases. Therefore, the data on the ice force before the first peak crushing stage were removed in the following analysis. Due to the different ice velocities, the interaction times differ. The same sea ice breaking length after the first peak at different velocities was selected as the interaction time period for the data analysis.

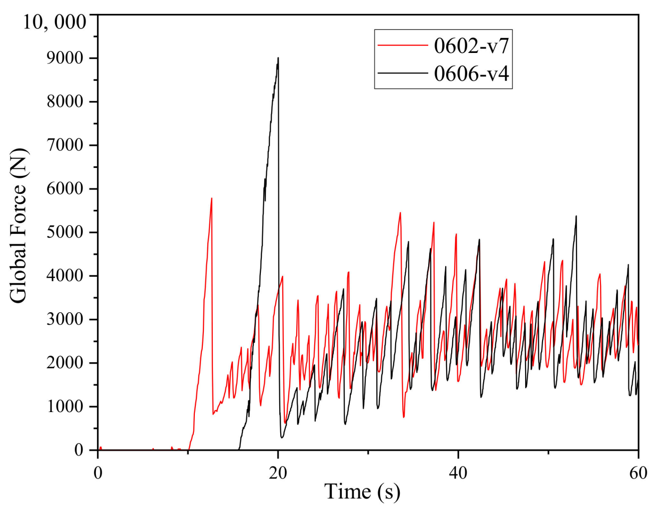

Figure 4. Total forces when V_{load} equals 4 mm/s and 7 mm/s.

By comparing the total ice sheet loading length at different velocities, the interaction times when the ice sheet breaking length is approximately 210 mm after the first peak were selected. The loading length is less than 210 mm when V_{load} is 1 mm/s, so the measured data at 60–180 s were extracted. For the other loading velocities, the loading time period with a loading length of approximately 210 mm was selected (as shown in Figure 5). The start time in the selected period was recorded as $T_{str,}$ and the end time was recorded as T_{end} (as shown in Table 2). Some measured data on the ice force and pressures were obtained in the selected period (including the peak value of the global ice force F_{max}, the maximum LIP $p^{L}{}_{max}$, the average LIP $p^{L}{}_{ave}$, and the standard deviation of LIP $p^{L}{}_{std}$, as shown in Table 2).

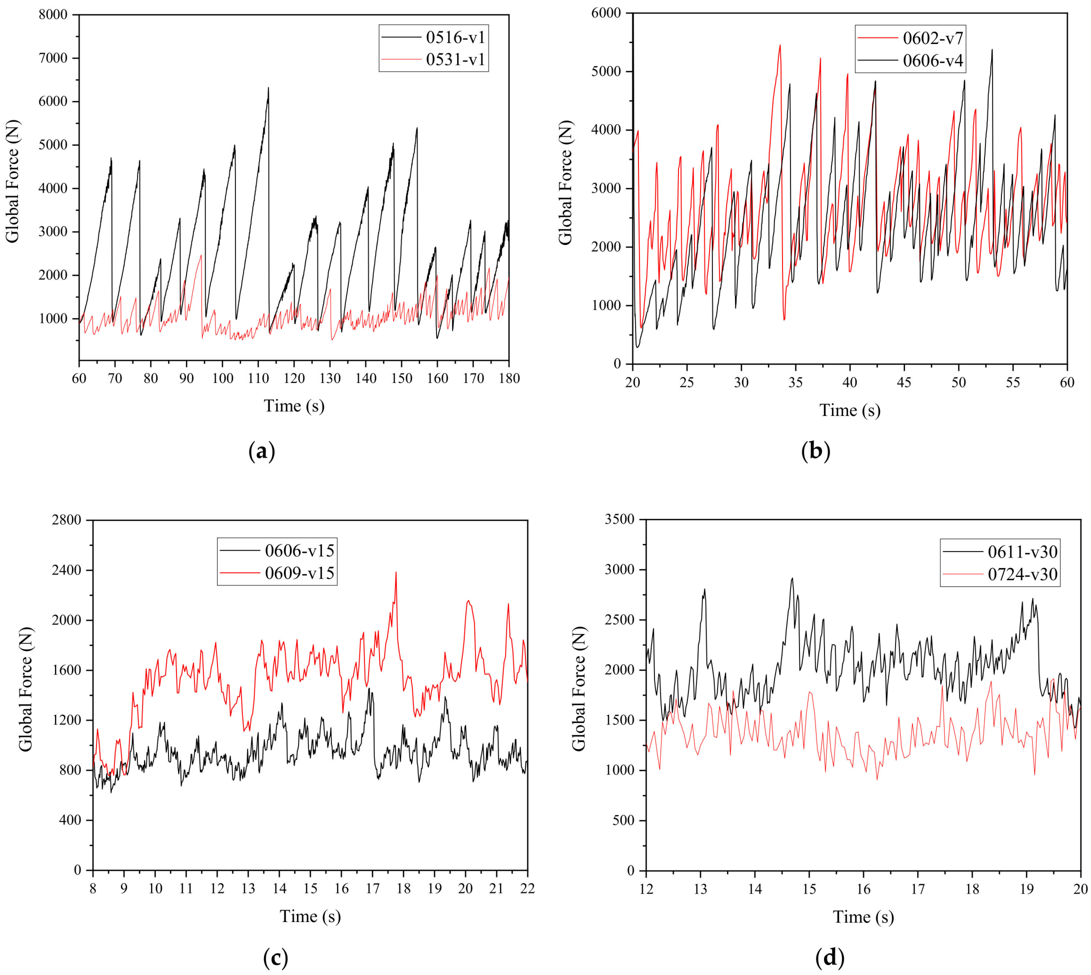

Figure 5. Selected global ice force curves. (**a**) V_{load} is 1 mm/s, (**b**) V_{load} is 4 mm/s and 7 mm/s, (**c**) V_{load} is 15 mm/s, (**d**) V_{load} is 30 mm/s.

Table 2. Measured global ice force and local ice pressure data.

Specimen	T_{str} (s)	T_{end} (s)	F_{max} (kN))	$p^{L}{}_{max}$ (MPa)	$p^{L}{}_{ave}$ (Mpa)	$p^{L}{}_{std}$ (Mpa)
0516-v1	60	180	6.33	1.66	0.204	0.255
0531-v1	60	180	2.47	1.23	0.096	0.112
0602-v7	22	52	5.46	1.23	0.123	0.121
0606-v4	22	75	5.38	1.26	0.121	0.127
0606-v15	8	22	2.39	0.39	0.042	0.037
0609-v15	8	22	1.46	0.67	0.078	0.071
0611-v30	12	20	2.92	0.75	0.158	0.151
0724-v30	12	20	1.89	0.56	0.079	0.099

The global ice force curve in Figure 5 exhibits a typical periodic change in the form of triangular waves when the loading velocity is less than 7 mm/s. In the loading stage of the ice force, the loading curve shows the characteristics of a linear increase and unloading to the minimum value immediately after reaching the peak value (as shown in Figure 5a,b). At loading velocities of 15 mm/s and 30 mm/s, there are several small loading-to-unloading processes during a complete loading-to-unloading cycle on the global ice force curve. The global ice force curves are mostly in the form of wavy lines during a complete loading-to-unloading period (as shown in Figure 5c,d). The differences in the loading curves at different velocities are mainly due to the different failure modes of the ice sheet. Ductile failure at low velocities results in more contact between the ice and the structure, and brittle failure at high velocities results in more frequent non-simultaneous failure of the local area and local unloading throughout the loading process.

4. Results and Discussion

4.1. Distribution Area of LIPs

To study the distribution law of HPZs along the ice thickness, a statistical analysis of LIPs in the time period discussed above (from T_{str} to T_{end}) is performed in this section. σ_{L} is a threshold value, it is used to describe the area of LIP greater than this value. The value of σ_{L} was determined as a multiple the average uniaxial compression strength (σ_{cr}). This multiple is represented by the threshold coefficient k_{t} ($k_{\mathrm{t}} = \sigma_{\mathrm{L}}/\sigma_{\mathrm{cr}}$, taken as 0.5, 0.7, 1.0, 1.5, 2.0, 2.5, 3.0). Taking the threshold σ_{L} as the limiting condition, the LIPs at each time and each location measured by the sensor were counted. When the LIP value is greater than or equal to the threshold limit σ_{L}, the count is increased by one; otherwise, the count remains constant and is expressed by the function $N(k_{\mathrm{t}})$.

$$N_j(k_t) = Num(P_j^{\mathrm{L}} \geq \sigma_{\mathrm{L}}) \;\; (j = 1,\, 2,\, 3\ldots, R) \tag{1}$$

$$Z_j(k_t) = \frac{N_j(k_t)}{M_s} \;\; (j = 1,\, 2,\, 3\ldots, R) \tag{2}$$

where P_j^{L} is the LIP measured by the jth local pressure sensor; N_j is the number of P_j^{L} greater than or equal to σ_{L}; R is the total number of local pressure sensors in the nominal contact area (NCA); Z_j is the probability of occurrence at different locations of the contact surface when the LIP is greater than or equal to the threshold coefficient k_{t}; and M_s is the total number of LIPs at each contact location measured by the sensor from T_{str} to T_{end}. The probability contour maps of the pressure distribution area in the NCA were determined for various velocities. The color bar indicates the value of Z_j (as shown in Figure 6).

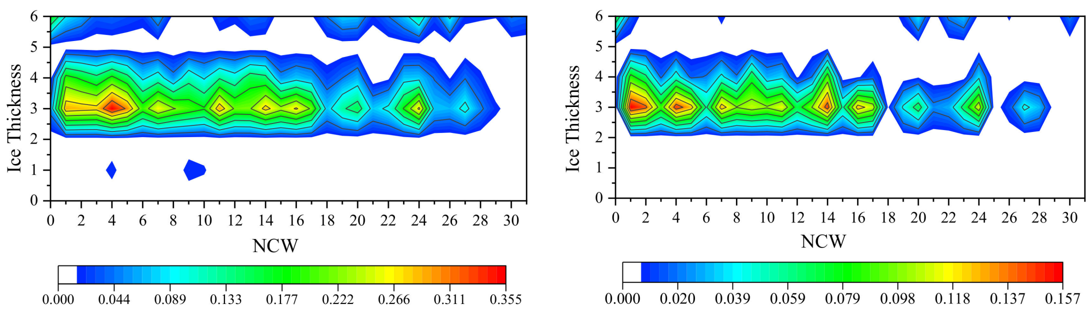

(a) (b)

Figure 6. *Cont.*

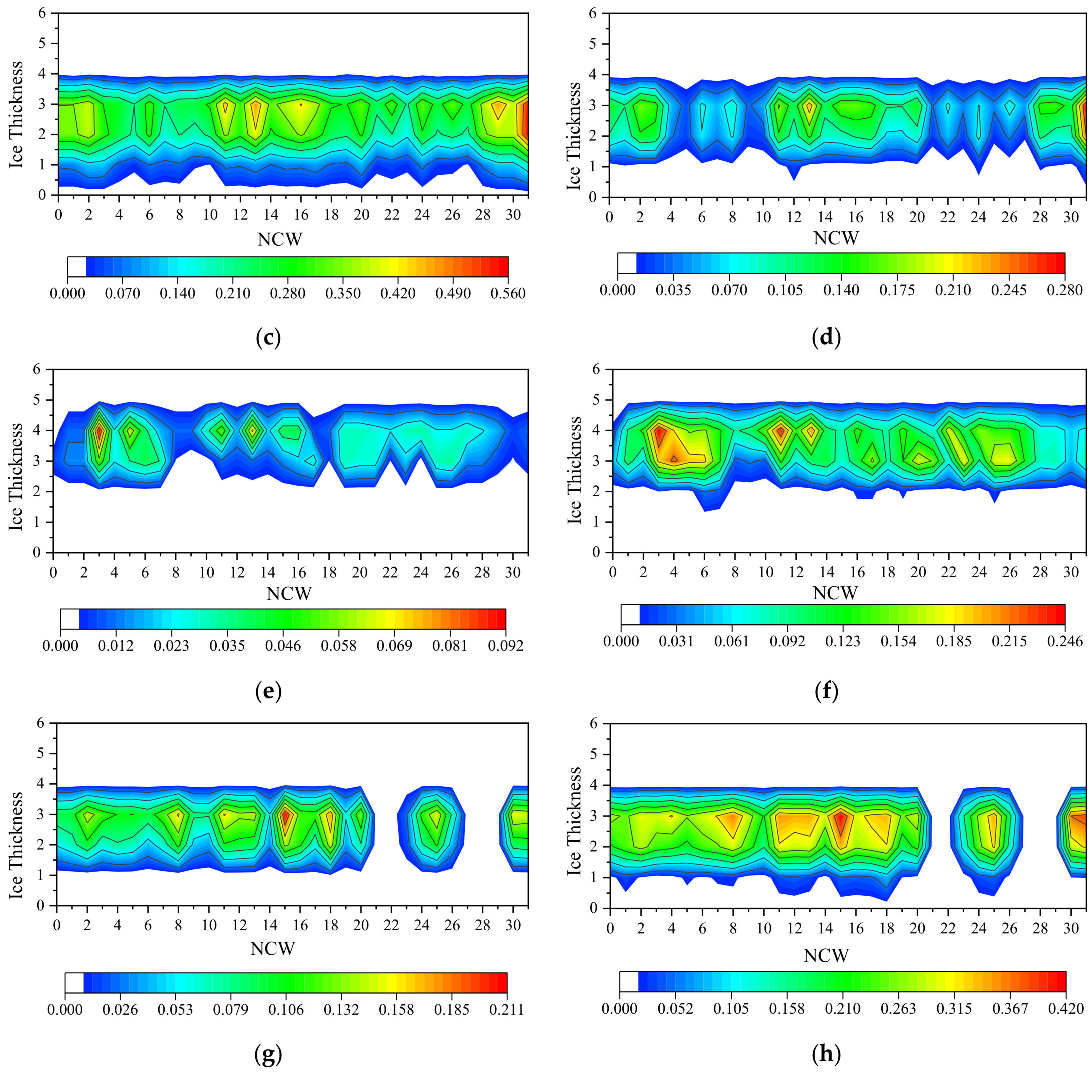

Figure 6. Probability contour maps of the LIP distribution area on the NCA at various velocities. (**a**) V_{load} is 1 mm/s and k_t is 1.0; (**b**) V_{load} is 1 mm/s and k_t is 1.5; (**c**) V_{load} is 7 mm/s and k_t is 1.0; (**d**) V_{load} is 7 mm/s and k_t is 1.5; (**e**) V_{load} is 15 mm/s and k_t is 1.0; (**f**) V_{load} is 15 mm/s and k_t is 0.7; (**g**) V_{load} is 30 mm/s and k_t is 1.0; (**h**) V_{load} is 30 mm/s and k_t is 0.7.

According to the probability contour maps of the LIP on the contact surface, the HPZs at various loading velocities and threshold coefficients k_t are distributed near the center of the ice thickness. The blue to red areas in the figure indicates the probability of the local pressure exceeding σ_L, ranging from low to high probabilities. The contour map shows that closer to the center, the probability distribution of the LIPs is higher (as shown in Figure 6. The area of all the colored areas in Figure 6 is defined as A_L, and the whole NCA is defined as A_{NCA}. When the same threshold coefficient k_t is used, the local pressure distribution area accounts for a large portion of the NCA at lower loading velocities (1 mm/s, 4 mm/s and 7 mm/s), while the local pressure distribution area A_L accounts for a small portion of the NCA at higher loading velocities (15 mm/s and 30 mm/s). According to the analysis in Section 2, the sea ice mainly exhibits ductile failure at low loading velocities. The strain during failure is large, which increases the contact between the ice sheet and the indentor and causes the failure to be more simultaneous. At a high loading velocity, the main failure mode of the ice sheet is brittle failure, which results in a more irregular contact surface and makes the failure more non-simultaneous. The ratio of the LIP area to the NCA under different thresholds can be calculated (Equation (3)):

$$q(k_t) = \frac{A_{\mathrm{L}}(k_t)}{A_{\mathrm{NCA}}} \tag{3}$$

where q is the area ratio coefficient, and k_{t} is the threshold coefficient.

The analysis of the variation law of the area ratio coefficient q versus the threshold coefficient k_{t} is shown in Figure 7, and it can be observed that the area ratio coefficient q changes linearly with the threshold coefficient k_{t} at various velocities. When the coefficient k_{t} = 1.0, the coefficient q is approximately 0.5 at a low loading velocity and approximately 0.25 at a high loading velocity. This result indicated that HPZs subjected to pressures greater than σ_{cr} represent 1/2 of the NCA at low velocities (Figure 7a) and approximately 1/4 of the NCA at high velocities (Figure 7b). The HPZs are generally located near the centerline of the ice. Furthermore, HPZs subjected to pressures greater than 3 times σ_{cr} represent less than 2% of the NCA (Figure 8a) at low velocities, and HPZs subjected to pressures greater than 2.5 times σ_{cr} represent less than 1% of the NCA (Figure 8b) at high velocities. Dempsey et al. found that the HPZs appear to be confined to the middle third of the ice thickness [3]. The red dashed box in Figure 7a,b indicates that HPZs represent approximately 1/3 of the NCA. The corresponding threshold coefficient k_{t} is 1.5 at low loading velocities and 0.7 at high loading velocities. That is, an HPZ pressure greater than 1.5 times the average uniaxial compressive strength σ_{cr} is located in the middle third of the ice thickness at a low loading velocity, and an HPZ pressure greater than 0.7 times the average uniaxial compressive strength σ_{cr} is located in the middle third of the ice thickness at a high loading velocity. The distribution area of HPZs is determined by the threshold values and failure models.

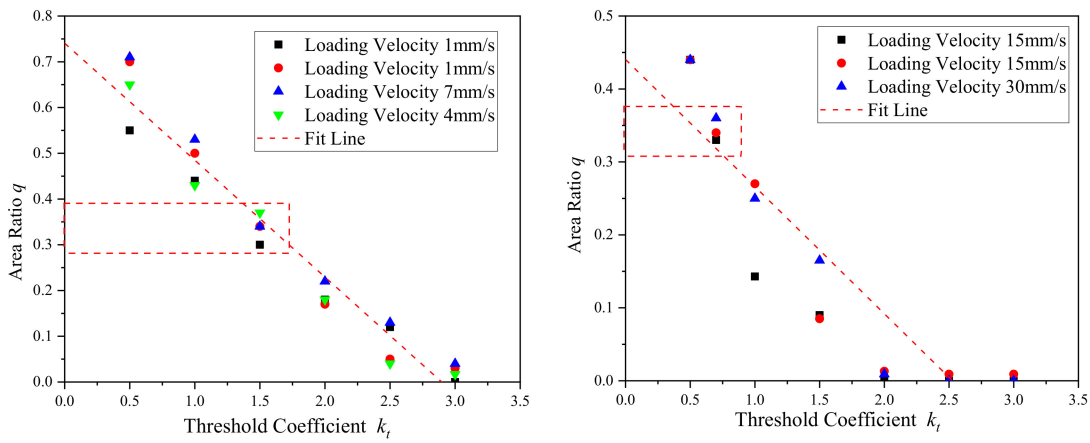

(**a**) (**b**)

Figure 7. Area ratio coefficient q versus threshold coefficient k_{t}. (**a**) V_{load} of 1 mm/s, 4 mm/s and 7 mm/s; (**b**) V_{load} of 15 mm/s and 30 mm/s.

Because the area ratio coefficient q versus threshold coefficient k_{t} varies linearly, a linear fitting formula (Equation (4)) was used to fit and analyze the data in Figure 7. The fitting parameters a and b are shown in Table 3. According to the above discussion, the HPZs are generally distributed in the centerline of the ice thickness. The distance of the HPZ edge from the ice thickness centerline can be calculated by Equation (5):

$$q(k_t) = \mathrm{b}k_t + \mathrm{a}\ (k_t > 0, q \geq 0) \tag{4}$$

$$W_d = \pm\frac{h_{ice}}{2}q(k_t) = \pm\frac{h_{ice}}{2}(\mathrm{b}\,k_t + \mathrm{a}) \tag{5}$$

where W_d is the distance of the HPZ edge from the ice thickness centerline when the threshold coefficient is k_t and h_{ice} is the ice thickness.

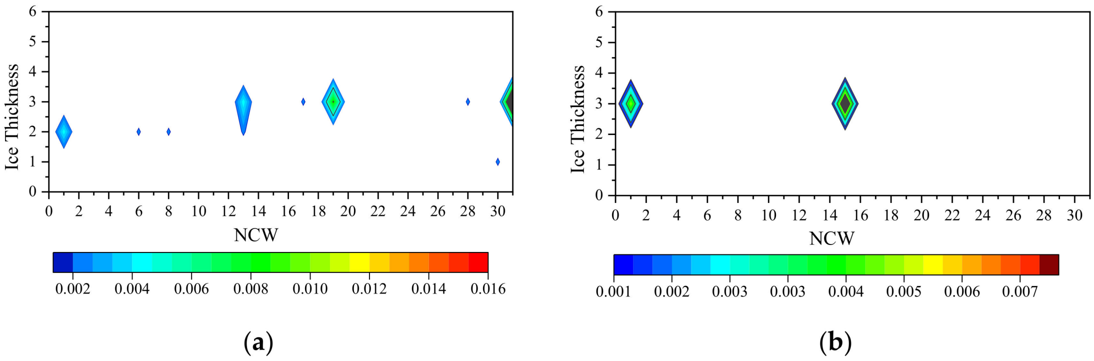

Figure 8. Less than 2% of HPZs located in NCA. (**a**) k_t is 3 and V_{load} is 1 mm/s; (**b**) k_t is 2 and V_{load} is 15 mm/s.

Table 3. The fitting parameters.

Failure	*a*	*b*	R^2
Ductile	0.741	−0.255	0.950
Brittle	0.44	−0.174	0.828

According to R^2 value (as shown in Table 3), it can be seen that the sea ice has a good fit when ductile failure occurs, and the R^2 is relatively small when brittle failure occurs, which indicates that the distribution of high-pressure area is more concentrated when ductile failure occurs.

The above discussion shows that the LIP distribution varies with the velocity, and the sea ice failure mode leads to the difference in the LIP distribution. The distribution area of the HPZs during brittle failure is smaller than that during ductile failure.

4.2. Probability Distribution of LIPs

The probability distribution of the LIPs in the time period discussed in Section 3 (from T_{str} to T_{end}) is determined in this section. The LIP value P_l measured by each local pressure sensor and the total number M_s of NCAs in the whole time period were obtained. The occurrence probability of P_l within each pressure value range was calculated at intervals of 0.01 MPa. P_i is the calculated value in the i-th step. P_1 is 0, and $P_{i+1} = P_i + 0.01$. The number of $P_i < P_l \leq P_{i+1}$ measured by the local pressure sensor is N_i, and the probability of Pr_i can be calculated by Equation (6):

$$\mathrm{Pr}_i(P_i < P_l \leq P_{i+1}) = \frac{N_i}{M_s}(i = 1,\ 2,\ 3\ldots) \quad (6)$$

The probability distribution histograms of the pressure value were determined for various loading velocities. The probability of LIPs decreases exponentially with increasing LIP. The probability of LIPs at various loading velocities follows a lognormal distribution (Figure 9). The lognormal function in Equation (7) was used to calculate the corresponding parameters of μ_s and σ_s at various loading velocities. The red lines in Figure 9 are the lognormal fitting lines based on Equation (7).

$$p(x) = A_s p_s(x) = \frac{A_s}{x\sigma_s\sqrt{2\pi}} e^{-\frac{(\ln \frac{x}{\mu_s})^2}{2\sigma_s{}^2}} \quad (7)$$

p(x) is fitting equation. $p_s(x)$ is probability density of LIP, A_s is the cumulative coefficient, x is LIP value. Because the selected interval is 0.01 MPa, *p(x)* is the area that reflects the composition of the y-axis and x-axis values, Since the area covered by the equation and x-axis is 0.01, in order to make the cumulative probability equal to 1, the coefficient A_s is 0.01. The parameters of the function at various velocities are shown in Table 4.

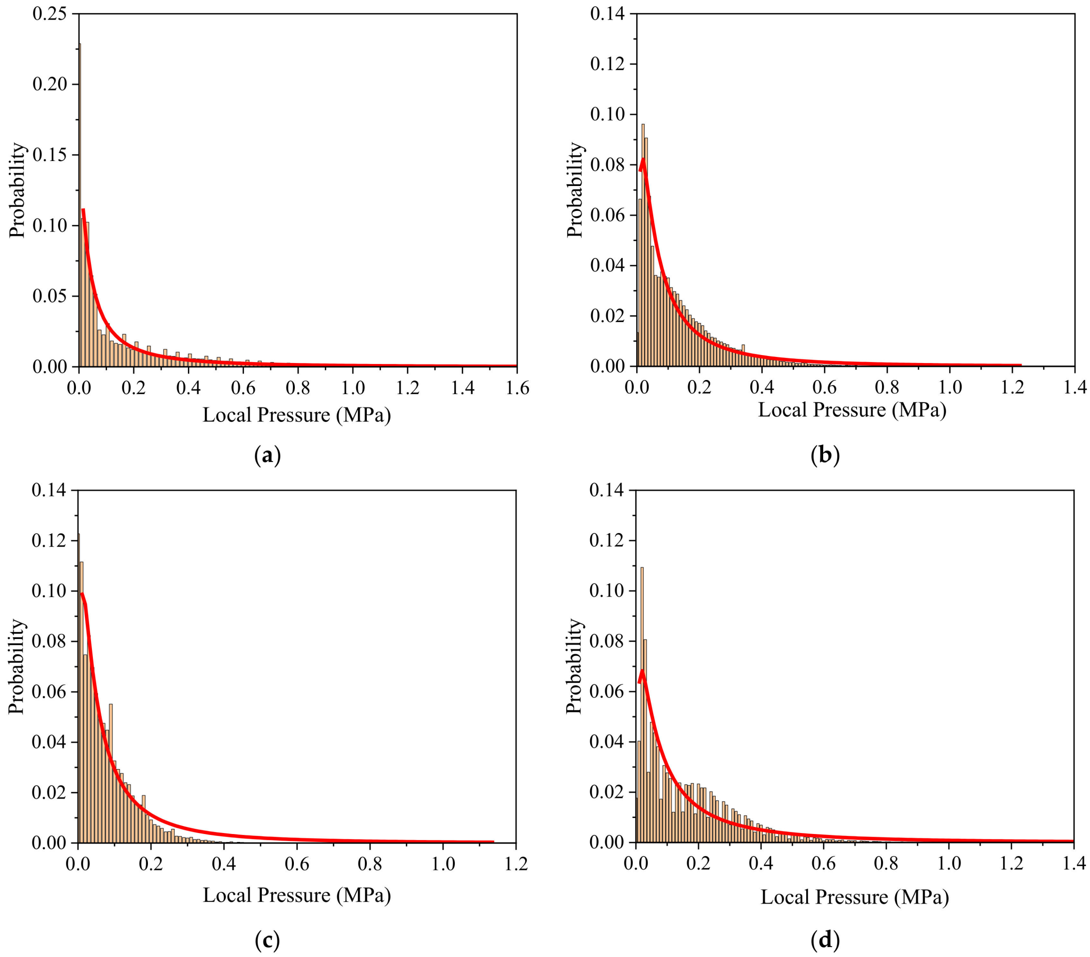

Figure 9. Local pressure versus probability. (**a**) V_{load} is 1 mm/s; (**b**) V_{load} is 7 mm/s; (**c**) V_{load} is 15 mm/s; (**d**) V_{load} is 30 mm/s.

Table 4. Parameters of the lognormal distribution at various velocities.

V_{load} (mm/s)	μ_s (MPa)	σ_s (MPa)	R^2
1	0.085	1.57	0.961
7	0.085	1.28	0.962
15	0.072	1.32	0.963
30	0.11	1.37	0.836

Table 4 shows that the μ_s ranges by approximately 0.04 MPa and σ_s ranges by approximately 0.3 MPa at various velocities. This indicates that the probability of LIP on the interaction surface between the ice sheet and indentor is similar across the whole action time at various velocities. When V_{load} is 1 mm/s, σ_s is greater than that under the other three loading velocities, which indicating that the local pressure fluctuates greatly. When V_{load} is 1 mm/s, μ_s is greater than that under the other three loading velocities. At this time, the non-simultaneous failure of ice sheet is obvious, the overall mean pressure is large and R^2 value is smaller than others. When V_{load} are 1, 7, 15 mm/s, the R^2 value is high, and the curve has a good fitting, which indicates that its distribution characteristics accord with lognormal distribution.

There is little difference in the local fatigue damage caused by LIPs at various velocities. The number of different pressures acting on the local area decreases exponentially with increasing pressure. The fatigue damage caused by the maximum LIP accounts for a small proportion of the total damage.

4.3. Spatial and Time Distribution Relationship

To study the spatial distribution of the LIP, LIP values were obtained at different moments during the loading and unloading processes of the global force. Figure 10a,b shows the selection method at low loading velocities (1 mm/s and 7 mm/s). Five time points of a complete loading and unloading cycle were selected: a. the initial loading moment; b. a moment during loading; c. the peak force moment; d. a moment during unloading; and e. the complete unloading moment. Figure 10c,d shows the selection method at high loading velocities (15 mm/s and 30 mm/s). The five time points during a complete loading and unloading cycle were: a. the initial loading moment; b. a small peak moment during loading; c. the peak force moment; d. a valley moment during unloading; and e. the complete unloading moment.

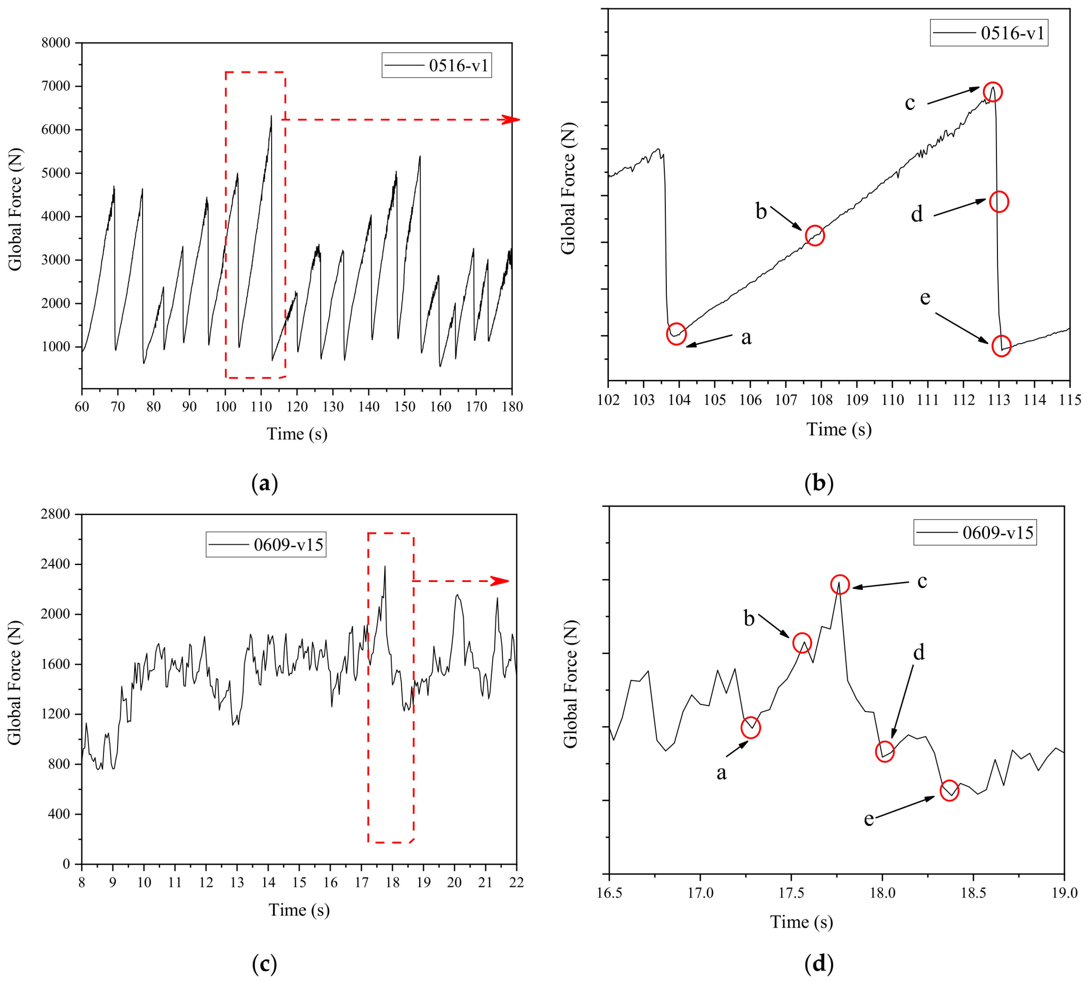

Figure 10. (**a**) Selected period from the global force when V_{load} is 1 mm/s; (**b**) five selected moments when V_{load} is 1 mm/s (a, b, c, d, e); (**c**) selected period from the global force when V_{load} is 15 mm/s; (**d**) five selected moments when V_{load} is 15 mm/s (a, b, c, d, e).

Figure 10a,b shows that the fluctuation of the global ice force curve in a single cycle is very small and tends to be loaded in a straight line. The global ice force curve presents a regular sawtooth shape, and the sea ice is periodically damaged at low velocities. At a low loading rate, the ice sheet shows ductile characteristics and a large strain, allowing sufficient contact on the width of the structure. The local failure of the ice sheet tends to be more simultaneous.

Figure 10c,d shows that the global ice force curve shows randomness and has no obvious periodicity. At a high loading rate, the ice sheet shows brittle failure. In the loading stage, there is a short time when the ice force declines in the curve, and failure occurs in some local areas. The failure section of the ice sheet is more irregular, and the failure in the contact width tends to be non-simultaneous. The sheet is continuously destroyed during the whole cycle on the contact width. The HPZs are concentrated in smaller local areas.

The LIP data at five moments (a, b, c, d, e) were extracted at various velocities. Table 5 shows the maximum LIP at five corresponding times (a, b, c, d, e) at each loading velocity. $p^L{}_{max}$ is the maximum LIP from T_{str} to T_{end} and $p^T{}_{max}$ is the maximum value at the five moments (a, b, c, d, e).

Table 5. The maximum LIP at five moments.

V_{load} (mm/s)	Maximum Pressure (MPa)						
	a	**b**	**c**	**d**	**e**	$p^T{}_{max}$	$p^L{}_{max}$
1	0.464	1.34	1.635	1.345	0.804	1.635	1.66
7	0.44	0.754	0.915	0.774	0.306	0.915	1.23
15	0.27	0.369	0.336	0.294	0.317	0.369	0.67
30	0.369	0.554	0.534	0.52	0.53	0.554	0.75

At low loading velocities (1 mm/s and 7 mm/s), Table 5 shows that $p^T{}_{max}$ appears at the peak moment of the global ice force in the loading cycle (moment c). The maximum pressure at the initial moment (moment a) and the complete unloading moment (moment e) are less than half of the value at the peak force moment (moment c). At high loading velocities (15 mm/s and 30 mm/s), Table 5 shows that $p^T{}_{max}$ appears at a small peak moment during loading (moment b). $p^T{}_{max}$ does not appear at the peak force moment time in the loading cycle (moment c). The maximum pressure at the initial moment (moment a) and the complete unloading moment (moment e) are less than half of the value at the peak force moment (moment c). The fluctuations of the local maximum ice pressure at the four moments in the whole loading cycle are small, and the range of the maximum ice pressure is within 20% (beginning at moment b). The occurrence of $p^T{}_{max}$ is affected by the failure mode of the ice sheet. When the failure mode of the ice sheet is mainly ductile failure, $p^T{}_{max}$ occurs at the peak force. $p^T{}_{max}$ can occur at any moment of the global ice force when the ice is mainly brittle failure.

From the heat figures of the LIP at five moments during the loading cycle (Figure 11), the spatial distribution characteristics of the LIP in the loading cycle can be analyzed.

Figure 11a,b show that the spatial distributions of LIPs at low velocities (1 mm/s and 7 mm/s) are similar. At the moments of loading (moment a) and unloading (moment e), the pressure distribution on the NCA is mainly in the blue pressure range (less than 1/8 times $p^T{}_{max}$). At the center of the ice thickness, there is a partial LIP range distributed at 2/8 to 3/8 times $p^T{}_{max}$. The $p^T{}_{max}$ value for the whole cycle occurs at moment c. The LIP distribution color in the figure is mainly green near the centerline, indicating that the LIP value is approximately 1/2 times the $p^T{}_{max}$; at the same time, there is a small amount of red in the figure of moment c. This result indicates that the area of the LIP value greater than 7/8 times the $p^T{}_{max}$ is less than 2% of the NCA. At a given moment on the contact surface between the ice and the structure, the number of HPZs is greater than the number of other local zones, which generally occurs in 1–3 pressure acquisition units. The above variation characteristics are shown in the width direction of the NCW, which indicates that the ice sheet fails at most positions along the NCW at the peak time (moment c).

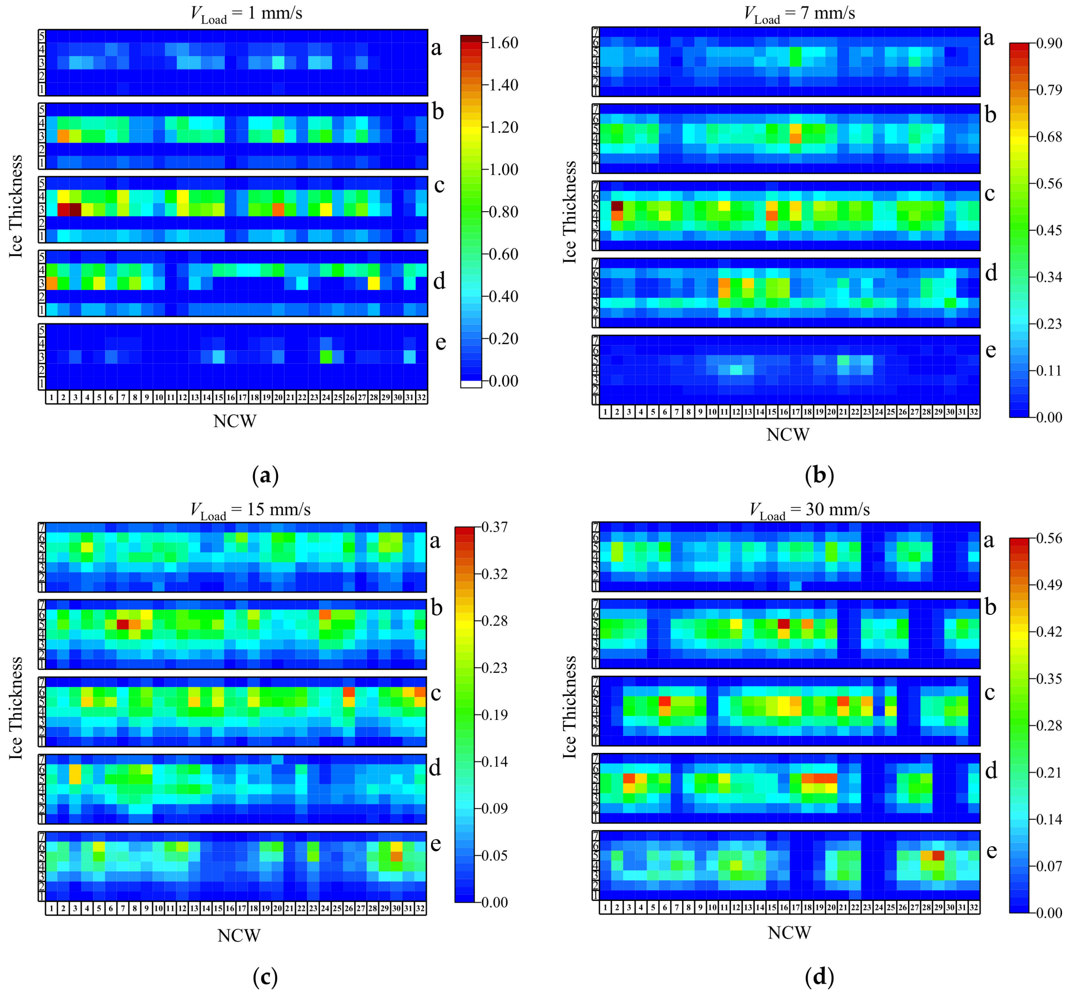

Figure 11. Distribution of local pressures in a period. (**a**) V_{load} is 1 mm/s; (**b**) V_{load} is 7 mm/s; (**c**) V_{load} is 15 mm/s; (**d**) V_{load} is 30 mm/s.

At high velocities (15 mm/s and 30 mm/s), a higher pressure was also distributed near the center of the ice thickness. In contrast to low loading velocities, the LIP distribution color is mainly green in the NCA from moment a to moment e at high loading velocities. A small number of red areas are distributed in the NCA from moment b to moment e. This indicates that there are HPZ values greater than 1/2 times p^{T}_{max} distributed throughout the cycle period and a few HPZ values greater than 7/8 times p^{T}_{max} (1–3 pressure acquisition units, less than 2% of the NCA) (as shown in Figure 11c,d)). There are some areas with alternating green and blue colors throughout the cycle period. For example, at a loading velocity of 30 mm/s, multiple blue areas at moment a become green areas at moment b and then become blue areas again at moment c. The above phenomena show that the sea ice in some areas fails at moments a and c, and fails in some areas at moment b along the width direction of the indentor at high velocities indicating non-simultaneous failure mode of the ice sheet.

5. Conclusions

The failure mode of the ice sheet is affected by the ice velocity. The sea ice experiences mainly ductile failure at low ice velocities and brittle failure at high ice velocities. Theoretical analysis of the interaction between the ice sheet and the vertical structure shows that the distribution of local ice pressures in the direction of the ice thickness differs under different failure modes. The indentation test verified the influence of the failure mode on the local ice pressure distribution at various velocities.

At low loading velocities, the global ice force curve presents a regular sawtooth shape, and the ice sheet has the same periodic loading-to-unloading characteristics at low velocities. In addition, the global ice force curve increases linearly during the loading stage. At high loading velocities, there are many small loading and unloading processes during a complete loading-to-unloading cycle, with most of the loading curves taking the form of random wavy lines.

The threshold coefficient k_t is taken as a multiple of the average uniaxial compressive strength σ_{cr}. When the coefficient k_t = 1.0, the coefficient q is approximately 0.5 at low loading velocities and approximately 0.25 at high loading velocities. The area ratio coefficient q changes linearly with the threshold coefficient k_t at various velocities. HPZs subjected to pressures greater than three times σ_{cr} represent less than 2% of the NCA at low velocities, and HPZs subjected to pressures greater than 2.5 times σ_{cr} represent less than 1% of the NCA at high velocities. The HPZs are distributed in a smaller area during brittle failure than during ductile failure at the same k_t. The probability distribution of the LIPs in local areas follows a lognormal distribution, and the ice velocity has little effect on the distribution probability.

At low loading velocities, as loading progresses during a loading cycle, the local extreme ice pressure increases. The local extreme ice pressure reaches its maximum at the moment that the global ice force reaches its peak. At high loading velocities, the $p^{T}{}_{max}$ in a loading cycle may appear at any moment of the global ice force. The maximum local ice pressure fluctuation at different moments is small throughout the loading cycle. The distribution of HPZs (greater than 7/8 times the $p^{T}{}_{max}$) accounts for less than 2% of the NCA. Only a few local areas are affected by highest LIP on the NCA.

Author Contributions: Conceptualization, G.W., Q.Y. and D.Z.; Data curation, G.W., Y.F. and X.P.; Formal analysis, D.Z., Y.F., X.P. and R.D.; Funding acquisition, D.Z.; Methodology, G.W. and D.Z.; Writing—original draft, G.W.; Writing—review & editing, G.W. and D.Z. All authors have read and agreed to the published version of the manuscript.

Funding: National Natural Science Foundation of China (grant number 52071055); The Innovation Team of Colleges and Universities 353 in Liaoning Province (grant number LT2019004).

Institutional Review Board Statement: Not applicable.

Informed Consent Statement: Not applicable.

Acknowledgments: This work was supported by the National Natural Science Foundation of China (grant number 52071055) and the Innovation Team of Colleges and Universities 353 in Liaoning Province (grant number LT2019004).

Conflicts of Interest: The authors declare no conflict of interest.

References

1. Cole, D.M. The microstructure of ice and its influence on mechanical properties. *Eng. Fract. Mech.* **2001**, *68*, 1792–1822. [CrossRef]
2. Wang, G.; Li, S.; Zi, L.; Zhang, D.; Xu, N.; Yuan, S.; Yue, Q.; Zhang, R. Influence factors of the uniaxial compression strength of sea ice. *J. Water Resour. Archit. Eng.* **2018**, *16*, 241–247.
3. Dempsey, J.P.; Palmer, A.C.; Sodhi, D.S. High pressure zone formation during compressive ice failure. *Eng. Fract. Mech.* **2001**, *68*, 1961–1974. [CrossRef]
4. Jordaan, I.J.; Maes, M.A.; Brown, P.W.; Hermans, I.P. Probabilistic analysis of local ice pressures. *J. Offshore Mech. Arct. Eng.* **1993**, *115*, 83–89. [CrossRef]
5. Sodhi, D.S. Crushing failure during ice–structure interaction. *Eng. Fract. Mech.* **2001**, *68*, 1889–1921. [CrossRef]
6. Wright, B.; Pikington, G.R.; Woolner, K.S.; Wright, W.H. Winter ice interactions with an arctic offshore structure. In Proceedings of the 8th IAHR Symposium on Ice, Iowa City, IA, USA, 18–25 August 1986.
7. Ralph, F. *Design of Ships and Offshore Structures: A Probabilistic Approach for Multi-Year Ice and Iceberg Impact Loads for Decision-Making with Uncertainty*; Memorial University: St. John's, NL, Canada, 2016.
8. Taylor, R.; Richard, M.; Hossain, R. A probabilistic high-pressure zone model for local and global loads during ice-structure interactions. *J. Offshore Mech. Arct. Eng.-Trans. ASME* **2019**, *141*, 051604. [CrossRef]
9. Sanderson, T.J.O. *Ice Mechanics and Risks to Offshore Structures*; Graham & Trotman: London, UK, 1988.

10. Frederking, R.; Timco, G.W.; Wright, B. Ice pressure distributions from first-year sea ice features interacting with the Molikpaq in the Beaufort Sea. In Proceedings of the International Offshore and Polar Engineering Conference, Brest, France, 30 May–4 June 1999.
11. Frederking, R. Ice pressure variations during indentation. In Proceedings of the 17th IAHR Ice Symposium, Saint Petersburg, Russia, 21–25 June 2004.
12. Karna, T.; Qu, Y.; Yue, Q.J. An extreme value analysis of local ice pressures. In Proceedings of the International Conference and Exhibition on Performance of Ships and Structures in Ice, Banff, AB, Canada, 16–19 July 2006.
13. Masterson, D.M.; Frederking, R.M.W. Local contact pressures in ship/ice and structure/ice interactions. *Cold Reg. Sci. Technol.* **1993**, *21*, 169–185. [CrossRef]
14. Timco, G.W.; Sudom, D. Revisiting the Sanderson pressure–area curve: Defining parameters that influence ice pressure. *Cold Reg. Sci. Technol.* **2013**, *95*, 53–66. [CrossRef]
15. Joensuu, A.; Riska, K. *Contact between Ice and Structure, Laboratory of Naval Architecture and Marine Engineering*; Helsinki University of Technology: Espoo, Finland, 1989. (In Finnish)
16. Jordaan, I.J. Mechanics of ice structure interaction. *Eng. Fract. Mech.* **2001**, *68*, 1923–1960. [CrossRef]
17. Hirayama, K.; Schwarz, J.; Wu, H. Model technique for the investigation of ice forces on structures. In Proceedings of the Second International Conference on Port and Ocean Engineering Under Arctic Conditions (POAC), Reykjavik, Iceland, 27–30 August 1973.
18. Kry, P.R. Scale effects in continuous crushing of ice. In Proceedings of the 5th International Association of Hydraulic Research Symposium on Ice Problems, Quebec City, QC, Canada, 27–31 July 1981.
19. Nakazawa, N.; Sodhi, D.S. *Ice Forces on Flat, Vertical Indentors Pushed through Floating Ice Sheets*; USA Cold Regions Research and Engineering Laboratory: Hanover, NH, USA, 1990; p. 70.
20. Saeki, H.; Ozaki, A. *Ice Forces on Piles*; Springer: Berlin/Heidelberg, Germany, 1980; pp. 342–350.
21. Zabilansky, L.J.; Nevel, D.E.; Haynes, F.D. Ice forces on model structures. *Can. J. Civ. Eng.* **2011**, *2*, 400–417. [CrossRef]
22. Sodhi, D.S. *Ice-Structure Interaction during Indentation Tests*; Springer: Berlin/Heidelberg, Germany, 1991; pp. 619–640.
23. Tanaka, S.; Saeki, H.; Ono, T. The distribution of ice pressure acting on offshore pile structure and the failure mechanics of ice sheet. *J. Offshore Mech. Arct. Eng.* **1987**, *109*, 85. [CrossRef]
24. Taylor, R.S.; Jordaan, I.J. Probabilistic fracture mechanics analysis of spalling during edge indentation in ice. *Eng. Fract. Mech.* **2015**, *134*, 242–266. [CrossRef]
25. Timco, G.W.; Weeks, W.F. A review of the engineering properties of sea ice. *Cold Reg. Sci. Technol.* **2010**, *60*, 107–129. [CrossRef]
26. Chen, X.; Wang, A.; Ji, S. The study on brittle-ductile transition mechanism and failure mode of sea ice under uniaxial compression. *Sci. Sin. Phys. Mech. Astron.* **2018**, *48*, 124601. [CrossRef]